JOURNAL OF SPACECRAFT AND ROCKETS
Vol. 46, No. 4, July–August 2009

Aerothermodynamic Testing of the Crew Exploration Vehicle at Mach 6 and Mach 10

Karen T. Berger*
NASA Langley Research Center, Hampton, Virginia 23681-2199

DOI: 10.2514/1.39247

An experimental wind-tunnel program is being conducted in support of a NASA wide effort to develop a Space Shuttle replacement and to support the agency's long-term objective of returning to the moon and Mars. This paper documents experimental measurements made on several scaled ceramic heat transfer models of the proposed Project Orion Crew Exploration Vehicle. The experimental data highlighted in this paper will be used to assess numerical tools that will be used to generate the flight aerothermodynamic database. Global heat transfer images and centerline heat transfer distributions were obtained over a range of freestream Reynolds numbers and angles of attack with the phosphor thermography technique. Temperature data were measured on the forebody and afterbody and were used to compute the heating on the vehicle as well as the boundary-layer state on the forebody surface. Several model support configurations were assessed to minimize potential aftbody support interference. Although naturally fully developed turbulent levels were not obtained on the forebody, the use of boundary-layer trips generated fully developed turbulent flow. Laminar and turbulent computational results are shown to be in good agreement with the data. In addition, the ability of the global phosphor thermography method to provide quantitative heating measurements in the low-temperature environment of the capsule base region was assessed and the lack of significant model support hardware influence on heating was shown.

Nomenclature

D	=	diameter, in.
H	=	Stagnation enthalpy, Btu/lbm
h	=	heat transfer coefficient $[\dot{q}/(H - H_w)]$, lbm/ft$^2 \cdot$ s
h_{ref}	=	reference heat transfer coefficient using Fay–Riddell calculation, lbm/ft$^2 \cdot$ s
k	=	boundary-layer trip height, in.
L_{ref}	=	reference length, in.
M_∞	=	Mach number
P_∞	=	pressure, psia
$\dot{q}$	=	heat transfer rate, Btu/ft$^2 \cdot$ s
q_∞	=	dynamic pressure, psi
Re_∞	=	unit Reynolds number (1/ft)
r	=	radius, in.
T_∞	=	temperature, °F
t	=	time, s
x	=	axial distance from origin, in.
α	=	angle of attack, deg
δ	=	boundary-layer height, in.
θ	=	boundary-layer momentum thickness, in.

Subscripts

aw	=	adiabatic wall
e	=	edge condition
$t, 1$	=	reservoir condition
$t, 2$	=	stagnation conditions behind normal shock
w	=	wall
1	=	freestream conditions
∞	=	freestream conditions

Presented as Paper 1225 at the 46th AIAA Aerospace Sciences Meeting and Exhibit, Reno, NV, 7–10 January 2008; received 20 June 2008; revision received 20 February 2009; accepted for publication 26 February 2009.

*Aerospace Engineer, Aerothermodynamics Branch, Mail Stop 408A. Member AIAA.

I. Introduction

THE Crew Exploration Vehicle (CEV), officially designated as Orion, is a blunt-body capsule that will ultimately be capable of transporting four crew members for lunar missions and later supporting crew transfers for Mars missions. In the near term, the CEV will be capable of transporting up to six crew members to and from the International Space Station. Despite the geometric simplicity of the basic Apollo-like capsule concept, many differences between CEV and Apollo remain. The CEV must be cost-effective and certain elements of the spacecraft must be reusable. To accommodate a greater crew complement, the crew module will be larger, with a heat-shield diameter approximately 30% larger than Apollo (16.5 vs 12.8 ft). The initial geometry, with a heat-shield diameter of 18.04 ft, is referred to as cycle I. Iterations on the geometry resulted in cycle II, with a diameter of 16.5 ft, truncation of the backshell length, and a reduction of the aft backshell radius. The cycle I geometry was used for this testing and is shown in Fig. 1.

To maintain a land-based recovery option while meeting disposal requirements of the service module before entry, the hypersonic trim angle of attack of the CEV was initially targeted at 152 deg. At the time of this research, the heat-shield design used a phenolic impregnated carbon ablator to protect the spacecraft during reentry into Earth's atmosphere as compared with Apollo's glass-phenolic ablative honeycomb heat shield. Similar to Apollo, pyrolysis/outgassing of the heat shield as it ablates during entry would occur. Boundary-layer transition to turbulent flow is likely to be induced earlier in the trajectory as compared with a nonablative heat shield, and significant material recession is anticipated. The thermal protection system (TPS) community has taken a conservative approach and is currently designing the heat shield for fully turbulent flow from the entry interface along the entire trajectory. Recent work indicates that the initial cycle I geometry and trim angle of attack may not be applicable, but because these initial experimental studies were designed for computational fluid dynamics (CFD) code validation, the data collected on the cycle I geometry at 152 deg are still valuable [the outer mold line (OML) and flight angle of attack are shown in Fig. 1b].

The primary objective of the test entry into the Langley Research Center (LaRC) 20-Inch Mach 6 Air Tunnel was to measure benchmark turbulent heating on the CEV heat shield. Test parametrics in Mach 6 include freestream unit Reynolds numbers of 2.1×10^6/ft–7.3×10^6/ft at a fixed angle of attack of 152 deg as

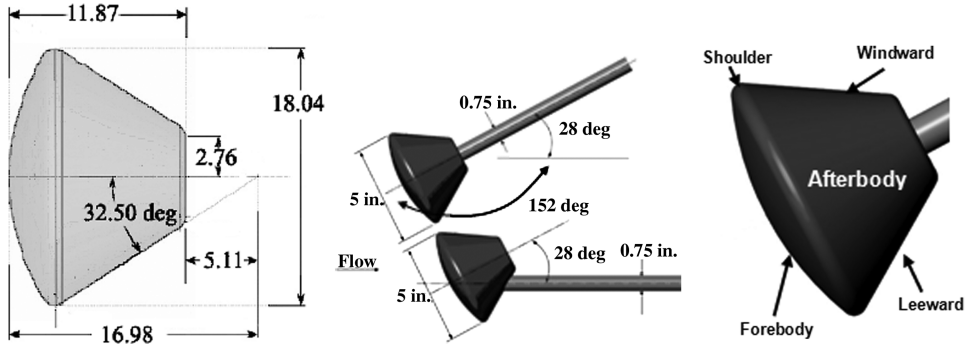

a) b) c)

Fig. 1 CEV cycle I OML and dimensions: a) full scale in feet, b) tunnel scale in inches, and c) model surface terminology.

well as a range of model diameters to increase length Reynolds numbers. A boundary-layer trip strategy was developed because fully developed turbulent heating could not be achieved naturally. Limited measurements on the CEV backshell were made to assess potential model support system interference on surface heating and to determine the response of the phosphor measurement technique in regions of low surface temperature.

The primary objective of the test entries into the LaRC 31-Inch Mach 10 Tunnel was to characterize the phosphor temperature response in a facility with a higher-temperature driver potential (and potentially higher signal-to-noise ratio and correspondingly lower measurement uncertainties than the Mach 6 facility). Measurements similar to those obtained in the Mach 6 tunnel were obtained to assess support system interference as well as the viability of testing the backshell surfaces in either facility. The higher heating levels in this facility, with corresponding lower uncertainties were desired for code validation on the backshell. Test parametrics in the Mach 10 facility include freestream unit Reynolds numbers of 1.0×10^6/ft–1.9×10^6/ft at a fixed angle of attack of 152 deg.

II. Experimental Methods

These experiments were completed in the NASA Langley Research Center's 20-Inch Mach 6 Air Tunnel and 31-Inch Mach 10 Tunnel. Descriptions of the models, wind tunnels, and global phosphor thermography system are presented.

A. Model/Support Hardware

Two model sizes, 5- and 7-in.-diam models, were tested in this study. The initial OML of the CEV crew module is a blunt-body capsule with a diameter of 18.04 ft, referred to as the cycle I OML. This diameter makes the 5- and 7-in.-diam tunnel models at 2.2 and 3.2% scale, respectively. A reference model OML is shown in Fig. 1. At the time of the initial model design, it was determined that all initial aerothermal CEV testing would use the cycle I geometry. Subsequent cycle II is a geometric scaling of cycle I from a diameter of 18.04 to 16.5 ft, a truncation of the backshell length, and a reduction on the radius on the aft backshell. The update from the cycle I to cycle II geometry did not affect the primary purpose of this testing.

The 5 and 7 in. cast ceramic models used in the Mach 6 and 10 test series were manufactured from molds created from rapid-prototyped resin patterns. Standard methods, materials, and equipment developed at LaRC were used in fabricating the ceramic aeroheating test models [1]. Specific model dimensions are shown in Table 1. All models were supported by cylindrical stings and one of two base-mounting techniques: 1) a straight sting mounted through the axis of symmetry and 2) a sting aligned 28 deg from the axis of symmetry to place the sting in the shadow of the flow (both shown in Fig. 1). Fiducial marks were applied to the model surface using a coordinate measuring machine. The reference marks on the model surface were used to align the model in the tunnel and to aid heat transfer data reduction.

The 5 in. models were mounted with both support hardware configurations. This procedure allowed for testing and imaging of the windward afterbody, largely mitigating the influence of the support hardware. All 7-in.-diam models were mounted with the straight sting only. All 5 in. models were mounted with 0.75-in.-diam stainless steel stings, and the 7 in. models were mounted with 1.0-in.-diam stainless steel stings.

B. Facility

The data included in this paper were obtained in the NASA Aerothermodynamics Laboratory. Both the 20-Inch Mach 6 Air Tunnel and 31-Inch Mach 10 Tunnel have well-characterized perfect-gas flows in terms of composition and uniformity. Nominal test conditions for the two facilities are shown in Table 2. Flow conditions were acquired using a 16-bit analog-to-digital facility acquisition system. The values of $P_{t,1}$ and $T_{t,1}$ are accurate to within $\pm 2\%$. The uncertainties in the angle of attack of the model are ± 0.2 deg.

The LaRC 20-Inch Mach 6 Air Tunnel [2] is a blowdown wind tunnel that uses dry air as the test gas and has a 20.5 by 20 in. test section. The maximum run time is 20 min with the ejector, though heating tests generally have total run times of 30 s, with actual model residence time on the tunnel centerline of approximately 5–10 s.

The LaRC 31-Inch Mach 10 Tunnel [2] is a blowdown wind tunnel that uses dry air as the test gas and has a 31 in. square closed test section. Facility run times of up to 2 min can be achieved, though heating tests generally have total run times of 30 s, with actual model residence time on the tunnel centerline of approximately 5–10 s.

C. Measurement Techniques

The two-color relative-intensity global phosphor thermography measurement technique [3–5] was used to obtain global experimental aeroheating data in the tunnel. This technique uses a mixture of phosphors that fluoresce in different bands of the visible spectrum

Table 1 CEV model nominal and measured dimensions

Cycle I	Nose cone radius, in.	Cone diameter, in.	Cone base diameter, in.	Total cone length, in.	Cone angle, deg	Front shoulder radius, in.	Base shoulder radius, in.
5 in. model nominal	6.000	5.000	1.780	3.290	32.500	0.250	0.250
5 in. model straight sting	5.989	4.962	1.788	3.271	32.387	0.239	0.229
5 in. model 28 deg sting	5.990	4.969	1.785	3.290	32.326	0.241	0.220
7 in. model nominal	8.400	7.000	2.493	4.603	32.500	0.350	0.350
7 in. model straight sting	8.390	6.948	2.491	4.593	32.373	0.318	0.368

Table 2 Nominal test conditions for 20 in. Mach 6 and 31 in. Mach 10 air tunnels

Tunnel	Test gas	$P_{t,1}$, psi	$T_{t,1}$, °R	P_∞, psi × 10^2	T_∞, °R	q_∞, psi	V_∞, ft/s	M_∞	Re_∞, $Ft^{-1} \times 10^{-6}$	Re_2, $ft^{-1} \times 10^{-5}$	P_2/P_∞	$P_{t,2}$, psi
Mach 6	Air	29	868	2.14	111.6	0.514	3020	5.86	0.533	0.934	5.25	0.956
Mach 6	Air	59	882	4.238	111.7	1.028	3047	5.88	1.046	1.83	5.26	1.91
Mach 6	Air	124	922	8.12	113.7	2.03	3122	5.98	1.98	3.422	5.28	3.772
Mach 6	Air	250	911	16.116	111.8	4.051	3103	5.99	4.043	6.933	5.28	7.528
Mach 6	Air	366	936	23.111	114.2	5.852	3142	6.02	5.632	9.724	5.29	10.876
Mach 6	Air	476	930	29.813	113.1	7.573	3136	6.04	7.383	12.651	5.29	14.073
Mach 10	Air	348	1800	0.992	95.2	0.65	4628	9.67	0.568	0.472	5.96	1.205
Mach 10	Air	723	1825	1.867	94.2	1.259	4670	9.81	1.104	0.898	5.98	2.334
Mach 10	Air	1452	1800	3.509	90.7	2.43	4643	9.94	2.24	1.755	5.98	4.503

when illuminated with ultraviolet light. The red and green bands are used and the intensity of the fluorescence is dependent upon the amount of incident ultraviolet light and the local surface temperature of the phosphor. This phosphor mixture, which is suspended in a silica ceramic binder and applied with an air brush, is used to coat a slip-cast-silica ceramic model. The final coating thickness is approximately 0.001 in. Using a 3-CCD (charge-coupled device) camera, fluorescence intensity images of an illuminated phosphor model exposed to the heated hypersonic flow of the tunnel are acquired and converted to temperature mappings via a temperature-intensity calibration. The temperature-intensity calibration uses the ratio of the red and green components of the image to construct a lookup table that converts the intensities to temperature value. This calibration is valid over a temperature range from 532 to 800°R. The temperature data from the time-sequenced images taken during the wind-tunnel run are then reduced to an enthalpy-based heat transfer coefficient h at every pixel on the image (and hence globally on the model) using a heat transfer calculation assuming one-dimensional semi-infinite slab heat conduction [4].

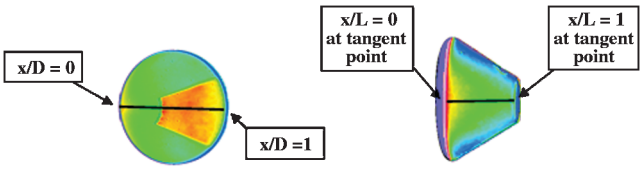

Fig. 2 Data format for forebody and afterbody phosphor testing.

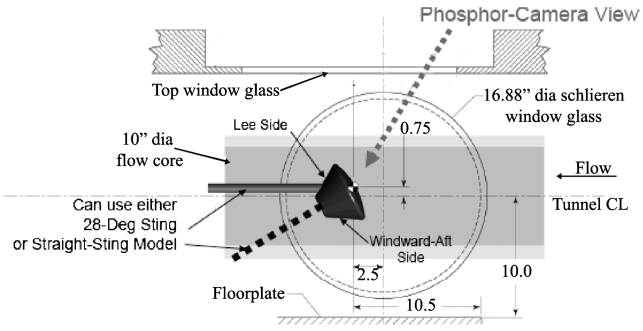

Fig. 3 Model setup in the 20-Inch Mach 6 Air Tunnel at NASA LaRC (dimensions in inches).

D. Data Presentation

Global heating images and the corresponding centerline data cuts will be presented in the x/D or x/L format for the forebody or afterbody, respectively (see Fig. 2). All heating data will be provided in the nondimensionalized h/h_{ref} format and are extracted from a two-dimensional image using fiducial-point locations. The reference h value is based on the Fay–Riddell hemisphere stagnation-point heating equation [6] with a nose radius of 6.0 or 8.4 in. for the 5- or 7-in.-diam models, respectively, and a cold-wall temperature of 540°R.

E. Data Quality/Uncertainty

Uncertainties in h with the phosphor thermography are based on surface temperature rise, and those presented here are based on historical testing with a variety of model types. On surfaces with significant temperature rise (60 + deg F), such as forebody surfaces, uncertainties are in the range of ±10%. For moderate temperature rise (20–30 deg F) such as the windward afterbody surface, the uncertainties are roughly ±25%. More information on uncertainties in the phosphor thermography can be found in [4,5].

III. Test Results

Test entries were completed in two tunnel facilities over a 6-month period. The purpose of these test entries was to assess the viability of aerothermal testing in the facilities and to generate a baseline set of heating data for the forebody and afterbody surfaces. The necessity for boundary-layer trips for forebody turbulent heating data was determined and a boundary-layer tripping strategy was developed. Nominal model installations can be seen in Figs. 3–6.

A. Tunnel Blockage Check

In general, a larger model size increases the likelihood of achieving naturally turbulent flow; however, tunnel flow blockage can be a concern for testing in both the 20 in. Mach 6 and 31 in. Mach 10 facilities. Although natural transition to turbulent heating levels was not expected in the Mach 10 tunnel due to the facility's Reynolds numbers range, the characterization of CEV model size limitations in the tunnel was motivated by a future desire to assess

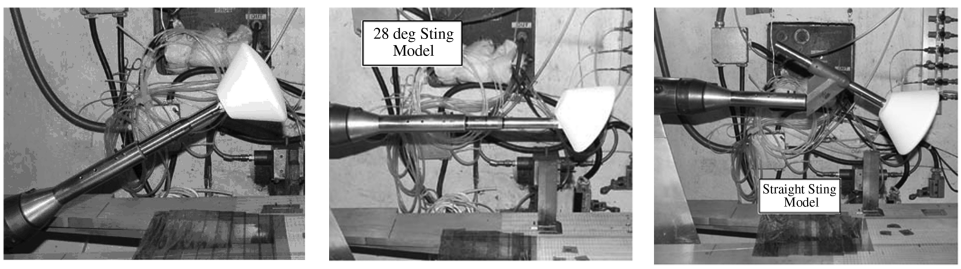

a) b) c)

Fig. 4 Model installation at the Mach 6 tunnel: a) forebody testing with the straight sting model, b) windward afterbody testing with the 28 deg sting model, and c) windward afterbody testing with the straight sting model.

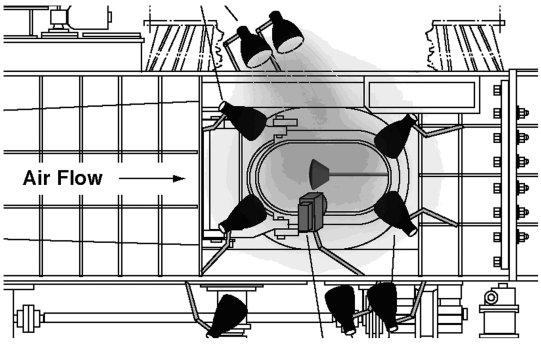

Fig. 5 Model setup in the 31-Inch Mach 10 Tunnel at NASA LaRC.

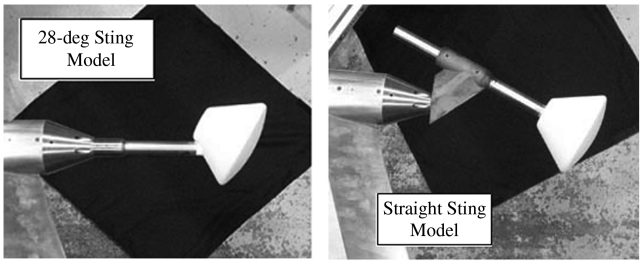

a) **b)**

Fig. 6 Afterbody heating installation at the Mach 10 tunnel; a) 28 deg sting model and b) straight sting model.

microaeroheating environments associated with penetrations and/or protuberances in the TPS. In the Mach 6 tunnel, a larger model scale permits higher-fidelity geometry associated with local deviations from the smooth OML in the form of window recessions or antenna fairings. In addition, a larger model enhances spatial resolution associated with potential interference heating from reaction control system jet interactions.

The 5- and 7-in.-diam models were tested in both facilities at the nominal angle of attack, 152 deg, as well as at a 180 deg angle of attack (heat-shield geometric stagnation point on the centerline of the tunnel) at low Reynolds numbers. From a facility performance perspective, a low Reynolds number condition with the model at a 180 deg angle of attack represents a worst-case bounding condition. The test core is the smallest at the lowest Reynolds number, and the projected model frontal area is the largest when the model is at a 180 deg angle of attack. If no signs of blockage are present at these conditions, then higher Reynolds numbers and/or angles of attack do not present tunnel blockage concerns. As shown in Table 3 (data are from the initial Mach 6 entry), wall pressure and Mach probe measurements in the Mach 6 tunnel show no indications of flow blockage due to model size. At all test conditions, the differences between the measured Mach probe data and the tunnel calibration information are less than 0.85%. A similar study was done in the Mach 10 tunnel with similar results. Based upon the current assessments performed in the LaRC Mach 6 and 10 tunnels, it was concluded that a diameter of 7 in. is viable in both facilities.

B. Laminar and Turbulent Heating Augmentation Levels

Only a few runs focusing on forebody heating were completed in the Mach 10 tunnel. Model support system constraints associated with the side injection system of the Mach 10 tunnel limit optical access and UV lighting of the CEV (forebody) heat shield. As expected, the model surface temperature on the heat shield exceeded the maximum temperature threshold of the phosphor at the upper Reynolds number range in this facility. At lower Reynolds numbers, regions away from the stagnation region did not saturate and a limited laminar heating distribution was obtained. In regions in which the data were obtained, compressibility effects were not evident between Mach 6 and 10, as shown in Fig. 7. Based on this study, future forebody testing using this support hardware system in the Mach 10 tunnel is not recommended, due to overscaling of the existing thermographic phosphor system over a large portion of the forebody, especially at the higher Reynolds numbers. Data issues associated with phosphor temperature saturation were not evident in the Mach 6 tunnel.

The primary objective of the Mach 6 test entry was to obtain turbulent data. For the purposes of the paper, transition onset is defined as the location at which the measured heating distribution departs from a laminar baseline. As expected, the measured heating distributions at the lower facility Reynolds numbers were essentially invariant with Reynolds number, indicative of laminar flow. As evident in Fig. 8, transition onset on the CEV heat shield was observed, but fully turbulent heating was not achieved (naturally) in the Mach 6 tunnel.

Because turbulent heating was not achieved naturally, a boundary-layer tripping strategy was developed during the initial test entry into the Mach 6 tunnel. The emphasis of the trip screening study was to determine a location and pattern that would ensure uniform turbulent heating over a substantial percentage of the heat shield. The isolated roughness elements used in the CEV trip study have evolved over the last decade [7]. In the manufacturing process, adhesively backed high-temperature tape is precut with a laser to the desired square planform shape. Height parametrics are controlled by the tape thickness. As shown in Fig. 9, fiducial marks were placed on the model surface to assist in the placement of the boundary-layer trips. The 0.05×0.05 in. protuberances on the model surface are analogous to a pizza box on a flat surface. Although this paper does not attempt to document the trip screening study, the test results are summarized in Fig. 10. It was quickly determined that the local spreading angle of turbulent flow behind a single isolated trip was very small ($\sim$10 deg). The footprint of the flow disturbance created by an individual isolated trip is shown as a region of increased heating.

It was determined that a single array of trips spaced approximately one trip length apart was most effective at producing a uniform turbulent heating pattern. The trip array was placed at an x/D

Table 3 Mach 6 tunnel flow-blockage information

Reynolds number ($\times 10^6$/ft)	Model	Angle of attack, deg	Mach probe measurement, psi	Tunnel calibration, psi	δ, psi	% difference
2.1	7 in.	180	3.898	3.881	0.017	0.43
2.1	No model	——	3.850	3.850	0.000	0.00
2.1	5 in.	152	3.853	3.829	0.024	0.64
2.1	7 in.	152	3.834	3.836	0.002	0.06
4.1	No model	——	7.534	7.555	0.021	0.27
4.1	5 in.	152	7.593	7.567	0.027	0.35
4.1	7 in.	152	7.572	7.563	0.009	0.12
5.6	No model	——	10.844	10.933	0.089	0.82
5.6	5 in.	152	10.971	10.925	0.046	0.42
5.6	7 in.	152	10.990	10.988	0.002	0.02
7.3	No model	——	13.907	13.997	0.09	0.65
7.3	7 in.	152	14.088	14.099	0.010	0.07
7.3	7 in.	152	13.942	13.981	0.039	0.28

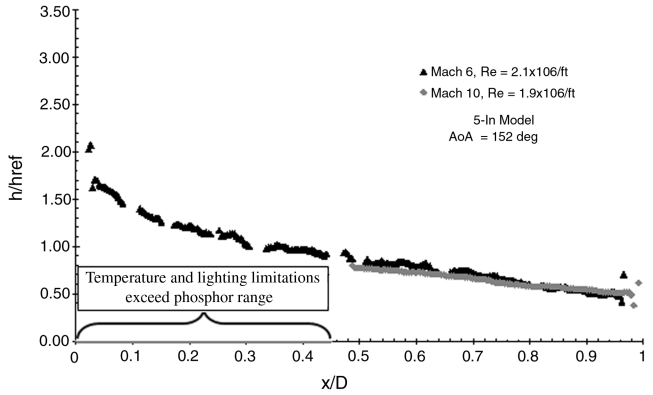

Fig. 7 Comparison of forebody heating in the Mach 6 and Mach 10 tunnels (AoA denotes angle of attack).

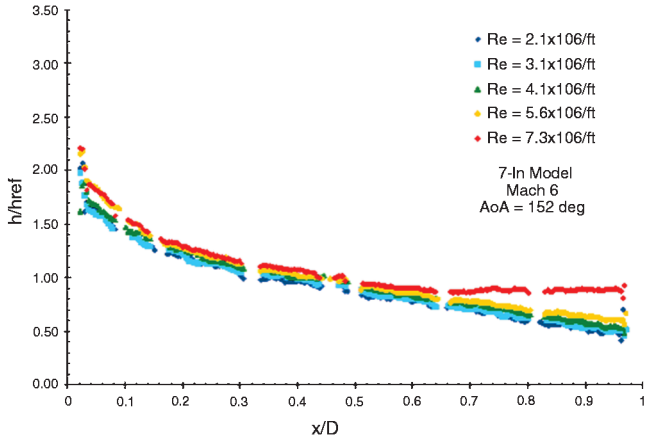

Fig. 8 Heating distribution over a range of Reynolds numbers (no trips).

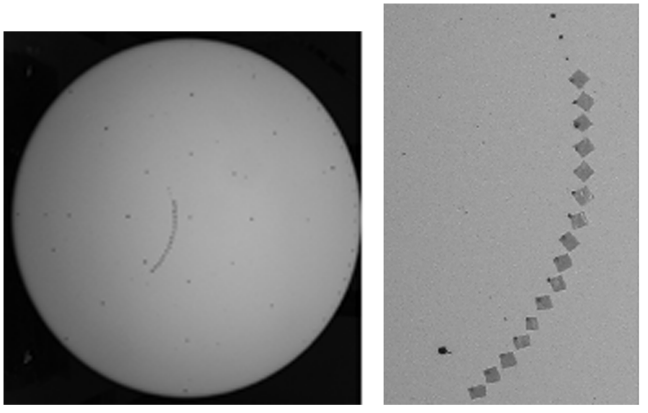

a) **b)**

Fig. 9 Fiducials and boundary-layer trip placement: a) boundary-layer trip array on model and b) close up view of boundary-layer trip array.

location of approximately 0.4, near the peak Re_θ/M_e value on the heat shield as determined by CFD pretest predictions.[†] The array crossed the centerline of the model but was not mirrored symmetrically on both sides, to allow for a direct comparison of untripped and tripped heating levels offcenterline during a single wind-tunnel run. Trip heights of 0.0045, 0.0065, and 0.0115 in. were tested and correspond to k/δ values of approximately 0.4, 0.6, and 1.05, respectively, at a unit Reynolds number of 7.3×10^6/ft.

In Figs. 11–13, heating distributions associated with three different boundary-layer trip heights are shown for freestream Reynolds numbers of 4.1, 5.6, and 7.3×10^6/ft, respectively. Fully turbulent flow was not achieved at the lower Reynolds number of 4.1×10^6/ft, as suggested by the lack of a peak heating region followed by a decreasing trend in the heating (a pattern evident in the data at the higher Reynolds numbers as well as in the predictions). Large heating peaks in the near wake of the trips were observed at all Reynolds numbers and are presumably associated with the initial vortical flow shed off of the trips. The smallest trip heights appeared to largely eliminate this overshot phenomena. As shown in Figs. 12 and 13, within approximately 20 trip lengths, the heating distributions at the two highest Reynolds numbers appeared to asymptotically approach consistent levels regardless of trip height and to decrease after peak heating, which is compelling evidence that the tripped flow has relaxed to equilibrium turbulent values at the higher Reynolds numbers. It is also noted that the experimental data matches pretest laminar and turbulent CFD predictions using the LAURA algorithm [8,9]. The predictions using the Cebeci–Smith turbulence model are computed for fully developed turbulent conditions as well as a condition in which the CFD prediction used an instantaneous transition from laminar to turbulent at a trip location of $x/D = 0.3$. It is of note that both predictions achieve the same heating levels as shown in Figs. 12 and 13. The predicted turbulent results are shown to be within 7% of the experimental measurements at the highest Reynolds number. As a matter of interest, when the two fully turbulent cases, 5.6×10^6/ft and 7.3×10^6/ft, are compared with the laminar cases around $x/L = 0.8$, the heating augmentation levels are 2.5 and 2.75, respectively.

C. Surface Visualization

Oil-flow surface visualization was used on the two different support hardware configurations tested in the Mach 10 tunnel. The straight sting model had a cylindrical sting concentric with the x axis, and the 28 deg sting model had a cylindrical sting offset by 28 deg from this axis and entering the model through the leeward afterbody surface. Blade mounts were not considered in this phase of the testing. Images of both the forebody and afterbody were taken postrun and used to help determine if there were any effects due to the support hardware configuration. Runs were made at Reynolds numbers of 1.0×10^6/ft and 1.9×10^6/ft. Images are shown in Figs. 14 and 15 for the $Re = 1.9 \times 10^6$/ft case. It is important to note that although the same procedure was used for each of the runs, each application of the oil and the paint will have some inherent differences, and so surface patterns associated with streamlines should be compared. Images were taken postrun and may have some effects of the gravitational pull on the oil and paint.

The patterns on the forebody are similar for the two configurations and show that there is no support hardware influence on the forebody surface of the model. On the windward afterbody, the line seen roughly one-third of the way from the front shoulder of the straight sting model is a result of oil/paint running from the forebody. The line near the base is a result of the gravitational pull on the oil and paint before the postrun image could be taken. The streamlines from the two different support hardware configurations do not exhibit any significant differences. There are differences to note on the leeside afterbody as a result of the support hardware location. In the area directly around the sting on the 28 deg sting model, the flow is disturbed. On the straight sting model, in the absence of the sting, the flow seems to remain almost stationary. These influences do not seem to feed onto the other surfaces of the model. The same general pattern can be seen on the two models as the windward afterbody is approached from the leeside. These oil-flow images show that there is not significant support hardware influence on the forebody or windward afterbody as a result of sting placement. The leeside afterbody is affected, but it is important to note that the measurement of the heating with phosphor thermography on the leeside of the 28 deg model is not possible, due to the sting location.

D. Windward Afterbody Support Hardware Comparisons

An objective of the wind-tunnel testing was to obtain information on the heating environment on the backshell to assess support

[†]Private communication with M. V. Pulsonetti, 6 January 2006.

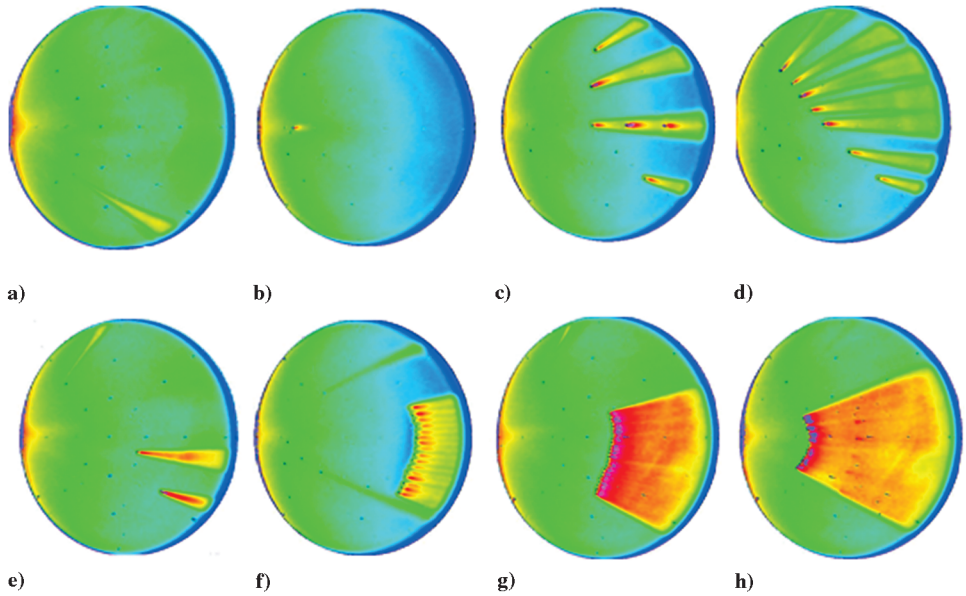

Fig. 10 Boundary-layer trip locations and orientations at 152 deg angle of attack and $Re = 7.3 \times 10^6/\text{ft}$: a) no boundary-layer trips with augmented heating as a result of surface coating damage, b) single trip at the stagnation point, c) 6 boundary-layer trips on the centerline and across the model, d) 7 boundary-layer trips in diagonal across the model, e) 2 offcenter trips at x/D locations of 0.6 and 0.8, f) boundary-layer trip array at $x/D = 0.8$, g) boundary-layer trip array at $x/D = 0.6$, and h) boundary-layer trip array at $x/D = 0.4$.

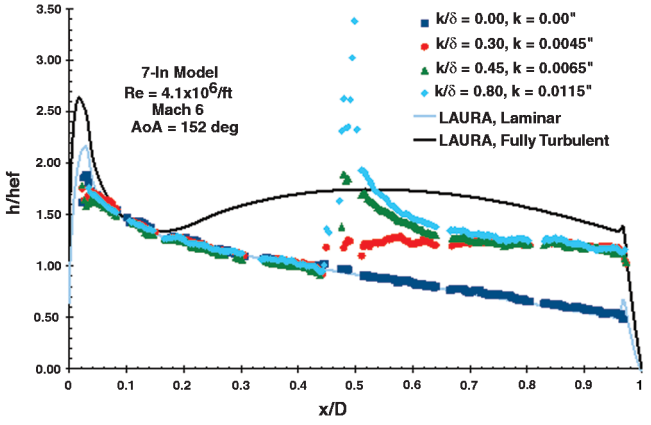

Fig. 11 Comparison of symmetry-plane experimental and predicted results at $4.1 \times 10^6/\text{ft}$.

hardware interference, compare with CFD results, and measure backshell heating levels. Two separate support hardware configurations were tested with the 5-in.-diam models to determine the influences on the afterbody heating associated with the sting placement. On the windward afterbody surface, it was expected that if there was influence, the 28 deg sting would exhibit less influence, as it would be completely shadowed within the wake flow when the model was pitched to the trim angle of attack of 152 deg.

A range of Reynolds numbers were run in the Mach 6 facility, and it was found that there was insufficient temperature rise (less than 5–10 deg) on the afterbody surface at the lower Reynolds numbers ($Re = 2.1 \times 10^6/\text{ft}$ and $4.1 \times 10^6/\text{ft}$) to obtain useful data. Figure 16 shows that at the higher Reynolds numbers there was a sufficiently high signal-to-noise ratio to obtain data. The two support hardware configurations exhibit the same heating levels, suggesting that there is no influence on the windward afterbody heating levels from the support hardware configuration.

Testing the afterbody in the Mach 10 tunnel is desirable due to the higher tunnel temperature and thus higher driving potential for implementing the thermographic phosphor system. Both of the sting configurations were tested, and just as in the Mach 6 tunnel, there was no significant difference in heating observed on the windward afterbody based on support hardware configuration. There was no evidence of Reynolds numbers influence on the two support hardware configurations (shown in Fig. 17). Similar conclusions can be made based on the computational results. It should be noted that the cause of the disagreement between experimental data and computational predictions near the shoulder of the model has not

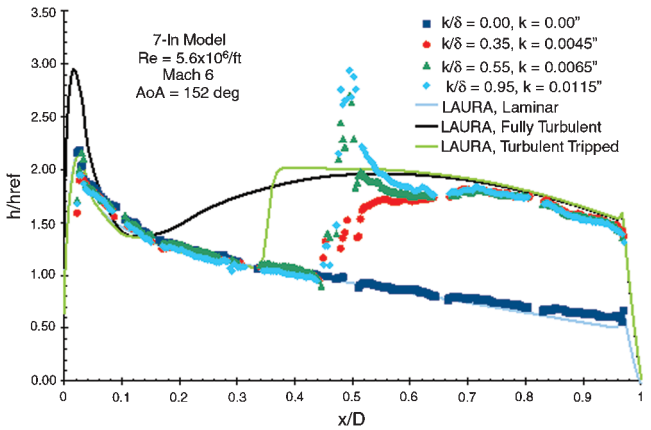

Fig. 12 Comparison of symmetry-plane experimental and predicted results at $5.6 \times 10^6/\text{ft}$.

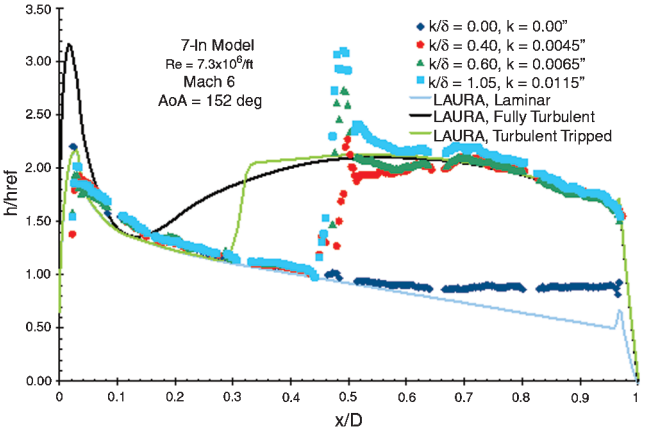

Fig. 13 Comparison of symmetry-plane experimental and predicted results at $7.3 \times 10^6/\text{ft}$.

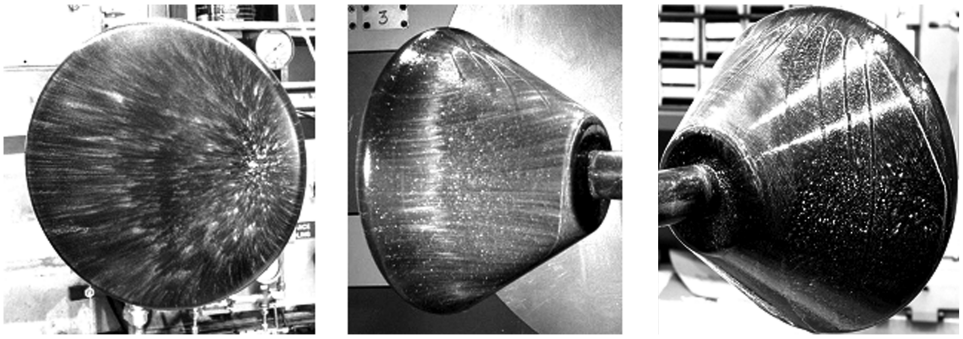

a) b) c)

Fig. 14 The straight sting model: a) forebody, b) windward afterbody, and c) leeside afterbody.

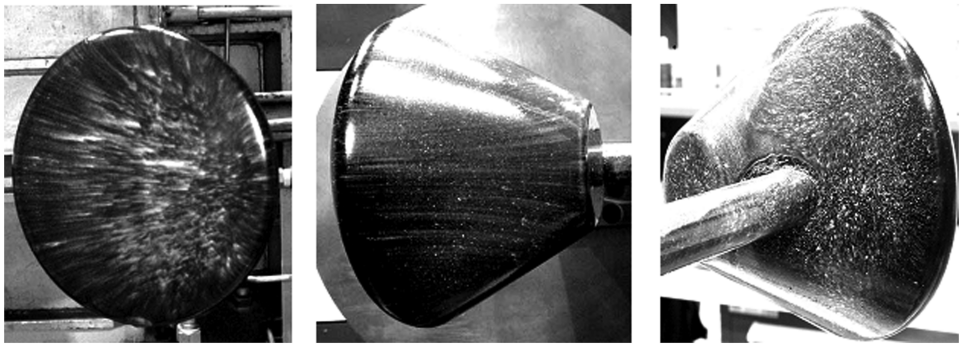

a) b) c)

Fig. 15 The 28 deg sting model: a) forebody, b) windward afterbody, and c) leeside afterbody.

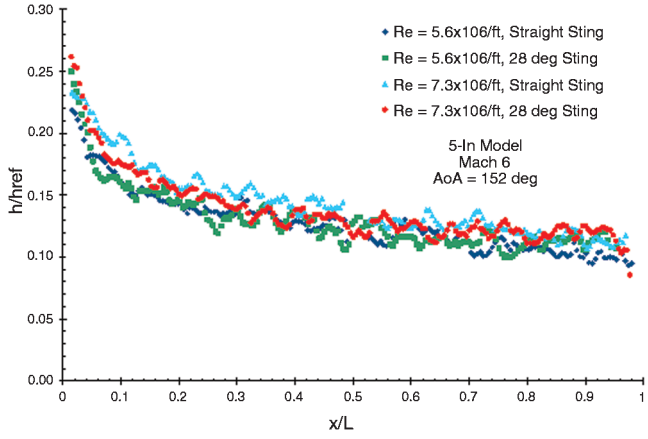

Fig. 16 Windward afterbody testing at Mach 6; straight and 28 deg sting models.

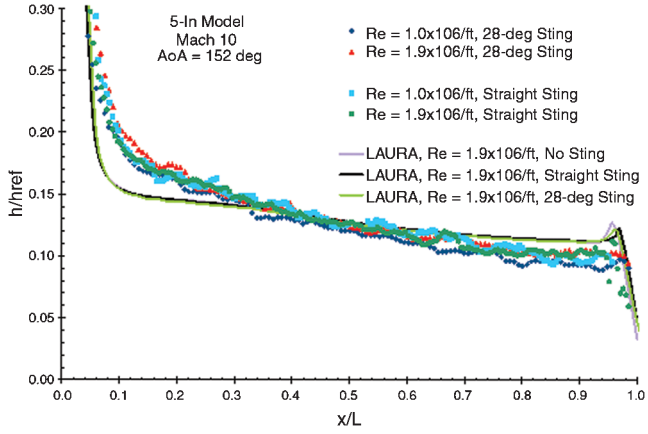

Fig. 17 Windward afterbody testing at Mach 10; straight and 28 deg sting models.

been identified. It is suspected that it may be the result of fabrication issues associated with the geometry of the corner (shown in Fig. 1c and associated with $x/L = 0$ in the data). The computational model incorporates a sharp corner and the experimental model may not be exactly the same in that region. Over the remainder of the windward afterbody surface, computational predictions seem to match well with the experimental results.

IV. Conclusions

Scaled models of the Crew Exploration Vehicle were tested in the LaRC 20 in. Mach 6 and 31 in. Mach 10 tunnels to obtain turbulent forebody heating data and afterbody heating data. The primary objectives of the experiment were to determine the suitability of the two facilities for aeroheating testing of CEV models and to obtain turbulent forebody heating data for comparison to computational predictions. Additional objectives were to determine the largest scale model that could be tested in the facilities and to determine any effects of the placement of model support hardware. The phosphor thermography system was used to obtain global heating images in both facilities. Oil-flow images were taken in the Mach 10 tunnel. All runs (with the exception of a limited number of blockage cases) were completed at the nominal flight angle of attack of 152 deg and Reynolds number ranges of 2.1×10^6/ft–7.3×10^6/ft and 1.0×10^6/ft–1.9×10^6/ft in Mach 6 and Mach 10 tunnels, respectively. Boundary-layer trips were necessary to ensure that the heating on the forebody in the Mach 6 facility was fully turbulent.

The experimental heating data collected with the phosphor thermography system were compared with computational predictions made with the LAURA code. On the forebody, heating rates at the two higher Reynolds number conditions match the predictions within 7% for the Mach 6 tunnel. Although both facilities were able to obtain afterbody heating data, the Mach 10 tunnel was more suited for the task, as the noise levels for the data were lower. With the exception of the shoulder region near $x/L = 0$, the experimental data compares well with the computational predictions. Both of the model scales that were tested in this series (2.2 and 3.2%) showed no signs of tunnel flow blockage and are allowable for testing. There were no

measurable effects of the support hardware configuration (straight sting or an offset sting) on the forebody or on the wind-side afterbody heating.

Acknowledgments

The author would like to thank the following people for their contributions to the project: Gary Wainwright, Mike Powers, Mark Griffith, Ed Covington, Pete Veneris, and Kathy Kuykendoll for their assistance in model design, fabrication, and preparation; Johnny Ellis, Paul Tucker, Anthony Robbins, Henry Fitzgerald, Grace Gleason, Harry Stotler, and Rhonda Mills for wind-tunnel support; Kevin Hollingsworth, Sheila Wright, and Teck-Sen Kwa for data acquisition assistance; Robert Nowak for test assistance; Thomas Horvath, Vincent Zoby, Randy Lillard, and Ben Kirk for assistance in data interpretation and understanding; Maria Pulsonetti, Frank Greene, and Steve Alter for LAURA computations. Without their help, these tests would not have been possible.

References

[1] Buck, G. M., Powers, M. A., Griffith, M. S., Hopkins, J. W., Veneris, P. H., and Kuykendoll, K. A., "Fabrication of 0.0075-Scale Orbiter Phosphor Thermography Test Models for Shuttle RTF Aeroheating Studies," NASA, TM-2006-214507, May 2006.

[2] Micol, J. R., "Langley Aerothermodynamics Facilities Complex: Enhancements and Testing Capabilities," AIAA Paper 98-0147, Jan. 1998.

[3] Buck, G. M., "Automated Thermal Mapping Techniques Using Chromatic Image Analysis," NASA, TM 101554, Apr. 1989.

[4] Merski, N. R., "Reduction And Analysis Of Phosphor Thermography Data with iHEAT Software Package," AIAA Paper 98-0712, Jan. 1998.

[5] Merski, N. R., "Global Aeroheating Wind-Tunnel Measurements Using Improved Two-Color Phosphor Thermography Model," *Journal of Spacecraft and Rockets*, Vol. 36, No. 2, 1999, pp. 160–170. doi:10.2514/2.3446

[6] Fay, J. A., and Riddell, F. R., "Theory of Stagnation Point Heat Transfer in Dissociated Air," *Journal of the Aeronautical Sciences*, Vol. 25, No. 2, 1958, pp. 73–85.

[7] Berry, S. A., and Hamilton, H. H., "Discrete Roughness Effects on Shuttle Orbiter at Mach 6," AIAA Paper 2002-2744, June 2002.

[8] Gnoffo, P. A., "An Upwind-Biased, Point-Implicit Relaxation Algorithm for Viscous Compressible Perfect Gas Flows," NASA TP 2953, Feb. 1990.

[9] Cheatwood, F. M., and Gnoffo, P. A., "User's Manual for the Langley Aerothermodynamic Upwind Relaxation Algorithm (LAURA)," NASA TM 4674, Apr. 1996.

B. Hollis
Associate Editor